J. Fluid Mech. (2012), *vol.* 692, *pp.* 137–152. © Cambridge University Press 2011
doi:10.1017/jfm.2011.500

Channel turbulence with spanwise rotation studied using helical wave decomposition

Yan-Tao Yang[1,2]† **and Jie-Zhi Wu**[2]

[1] Center for Applied Physics and Technology, College of Engineering, Peking University, Beijing 100871, China

[2] State Key Laboratory of Turbulence and Complex System, College of Engineering, Peking University, Beijing 100871, China

(Received 21 February 2011; revised 28 August 2011; accepted 9 November 2011; first published online 16 December 2011)

Turbulent channel flow with spanwise rotation is studied by direct numerical simulation (DNS) and the so-called helical wave decomposition (HWD). For a wall-bounded channel domain, HWD decomposes the flow fields into helical modes with different scales and opposite polarities, which allows us to investigate the energy distribution and nonlinear transfer among various scales. Our numerical results reveal that for slow rotation, the fluctuating energy concentrates into large-scale modes. The flow visualizations show that the fine vortices at the unstable side of the channel form long columns, which are basically along the streamwise direction and may be related to the roll cells reported in previous studies. As the rotation rate increases, the concentration of the fluctuating energy shifts towards smaller scales. For strong rotation, an inverse energy cascade occurs due to the nonlinear interaction of the fluctuating modes. A possible mechanism for this inverse cascade is then proposed and attributed to the Coriolis effect. That is, under strong rotation the fluctuating Coriolis force tends to be parallel to the fluctuating vorticity in the region where the streamwise mean velocity has linear profile. Thus the force can induce strong axial stretching/shrinking of the vortices and change the scales of the vortical structures significantly.

Key words: rotating turbulence, turbulence simulation, turbulence theory

1. Introduction

Rotation is of great interest in many natural and engineering flows. To investigate the effects of background rotation on wall-bounded flow, we focus on channel flow with spanwise rotation, i.e. channel rotates constantly around an axis pointing in the spanwise direction. This model problem has been studied extensively in the past. In such a flow, both the turbulence statistics and flow structures are dramatically changed from the non-rotating channel case. In a spanwise rotating channel, the mean velocity is in the streamwise direction, thus with constant rotation the Coriolis force associated with the mean velocity is normal to the walls. This Coriolis force points towards the wall at one side of channel, which is referred to as the pressure side. The other side

† Email address for correspondence: yytmech@pku.edu.cn

https://doi.org/10.1017/jfm.2011.500 Published online by Cambridge University Press

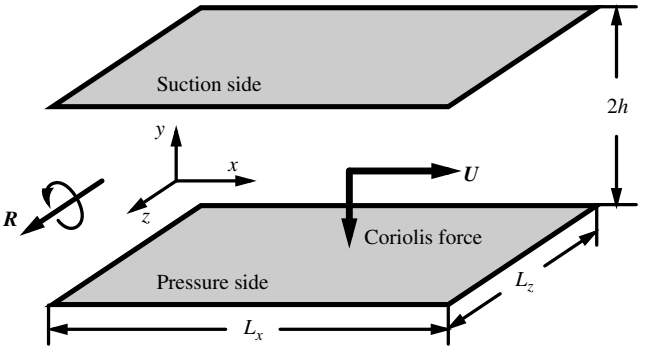


FIGURE 1. A schematic illustration of the channel with spanwise rotation.

is called the suction side since the force points away from the wall, see the sketch in figure 1. The experiments of Johnston, Halleen & Lezius (1972) have revealed that the flow exhibited very different properties at opposite sides of channel. Turbulence was enhanced at the pressure side and depressed at the suction side. In between, a linear segment appeared in the profile of the mean streamwise velocity. The slope of the linear segment was close to twice the angular speed of the system rotation, which implies that the absolute mean vorticity was near zero in this region (e.g. as shown in figure 3 below). Long counter-rotating roll cells were detected at the pressure side and extended to near the suction side. Recent experiments of Nakabayashi & Kitoh (2005) suggested that these paired roll cells created strong ejection from the pressure side to the suction side and thus made a large contribution to the transport of the Reynolds shear stress.

Kristoffersen & Andersson (1993) conducted direct numerical simulations (DNS) of spanwise rotating channel flow and compared the results with the experiments of Johnston *et al.* (1972). The large roll cells were also observed in the simulations and illustrated by the flow patterns on the cross-section after averaging in the streamwise direction and over time. The authors concluded that the roll cells shrank in size and increased in number as the rotation strengthened. Lamballais, Métais & Lesieur (1998) performed large-eddy simulation (LES) of the same flow and found that the roll cells only appeared at small rotation rates and tended to disappear for large rotation rates. The simulations of Takfti & Vanka (1991) indicated that the roll cells had important effects on the transport of the turbulent fluctuation from the pressure side to the suction side, and thus modified the turbulent structures significantly. Meanwhile, the two-dimensional base flow with spanwise rotation would lose stability and form streamwise vortices, see the experiments of Alfredsson & Persson (1989) and the instability analysis of Wall & Nagata (2006). The numerical simulation of Lamballais, Lesieur & Métais (1996) also implied that the streamwise roll cells could initiate the transition at moderate rotation rate.

More recently, Grundestam, Wallin & Johansson (2008) carried out a comprehensive DNS study of a spanwise rotating channel. They successfully achieved extremely high rotation rates. For a rotation rate higher than that in Kristoffersen & Andersson (1993), the roll cells were detected by the averaged flow patterns on the cross-section, although the patterns blurred after long time average. It was interesting that the turbulence statistics behaved non-monotonically with respect to the rotation rate. The wall-friction velocity at the pressure side first increased and then decreased as the rotation rate grew, while at the suction side it first decreased and then increased. For

https://doi.org/10.1017/jfm.2011.500 Published online by Cambridge University Press

the largest rotation number in Grundestam *et al.* (2008), the wall-friction velocities at two walls reached the same value and the turbulence was totally suppressed with the flow being relaminarized.

All these existing studies strongly suggest that large-scale structures exist at small rotation rates, but they are not found for large rotation rates. Thus the dominant scales of the flow structures seem to depend significantly on the rotation rate. In the present paper we will utilize the *helical wave decomposition* (HWD) to (*a*) clarify the dominant scale of flow structures for different rotation rates in spanwise rotating channel flow, and (*b*) explore the nonlinear energy transfer among different scales. HWD has been applied by Yang, Su & Wu (2010) to streamwise rotating channel flow and proved to be an excellent scale-decomposition tool for channel flow. The relevant dynamics in the physical space will also be investigated.

The paper is organized as follows. We briefly describe the theoretical formulation for spanwise rotating channel flow and HWD in § 2. Then we apply HWD to our DNS data in § 3, along with detailed discussions. A conclusion will be given in § 4.

2. Theoretical formulation

Figure 1 shows a schematic plot of the channel with spanwise rotation. Here (x, y, z) denote the streamwise, wall-normal and spanwise directions, and (u, v, w) the corresponding velocity components, respectively. The domain is set to be $(0, L_x) \times (-h, h) \times (0, L_z)$. In the rotating frame of reference, the Navier–Stokes (NS) equation for the incompressible flow reads, with unit density,

$$\frac{\partial \boldsymbol{u}}{\partial t} + \boldsymbol{l} + 2\boldsymbol{R} \times \boldsymbol{u} = -\nabla P_m + \nu \nabla^2 \boldsymbol{u}, \tag{2.1}$$

where $\boldsymbol{l} = \boldsymbol{\omega} \times \boldsymbol{u}$ is the Lamb vector with $\boldsymbol{\omega}$ the vorticity field, $\boldsymbol{R}$ is the angular velocity of the system rotation, P_m is the modified pressure, including the static pressure, kinetic energy and potential of the centrifugal force, and ν the kinematic viscosity. The last term on the left-hand side is the Coriolis term. For spanwise rotation we have $\boldsymbol{R} = R\boldsymbol{e}_z$ with $\boldsymbol{e}_z$ being the spanwise unit vector. Two important non-dimensional parameters, the Reynolds number and the rotation number, are defined as

$$Re = \frac{Uh}{\nu} \quad \text{and} \quad Ro = \frac{2Rh}{U}, \tag{2.2}$$

with U being some characteristic velocity. Ro is the ratio of the Coriolis effect to the inertial convection. Larger Ro means stronger rotation.

HWD will be used to analyse the flow fields and dynamic equations. A systematic background has been given in Yang *et al.* (2010), of which the basic ideas are outlined here. Suppose a solenoidal vector field $\boldsymbol{v}$ defined over domain $\mathscr{D}$ satisfies the non-penetration boundary condition on the domain boundary $\partial\mathscr{D}$, i.e. $\boldsymbol{n} \cdot \boldsymbol{v} \equiv 0$ with $\boldsymbol{n}$ being the outward normal vector. Then $\boldsymbol{v}$ can be decomposed by HWD into helical modes with different wavenumbers and opposite polarities:

$$\boldsymbol{v}(\boldsymbol{x}) = \sum_{s,\boldsymbol{k}} \widehat{v}_s(\boldsymbol{k}) \boldsymbol{\phi}_s(\boldsymbol{k}, \boldsymbol{x}), \tag{2.3}$$

where $s = \pm 1$ is the polarity index and $\boldsymbol{k}$ the wavenumber vector; the $\widehat{v}_s$ are the helical coefficients and $\boldsymbol{\phi}_s(\boldsymbol{k}, \boldsymbol{x})$ are the helical bases. Hereafter a hat denotes the helical coefficient. Note that for incompressible flow both the velocity and vorticity fields are naturally divergence-free and have zero wall-normal components at any stationary and

https://doi.org/10.1017/jfm.2011.500 Published online by Cambridge University Press

non-slip boundary, thus they can be directly decomposed by HWD. For the nonlinear Lamb vector $\boldsymbol{l}$, one can still use HWD after conducting the Helmholtz decomposition.

The helical bases $\boldsymbol{\phi}_s(\boldsymbol{k},\boldsymbol{x})$ are actually the eigenfunctions of the curl operator over $\mathscr{D}$ associated with the eigenvalues sk with $k=|\boldsymbol{k}|$:

$$\boldsymbol{\nabla}\times\boldsymbol{\phi}_s(\boldsymbol{x})=sk\boldsymbol{\phi}_s(\boldsymbol{x}) \quad \text{on } \mathscr{D}, \tag{2.4}$$

$$\boldsymbol{n}\cdot\boldsymbol{\phi}_s(\boldsymbol{x})=0 \quad \text{on } \partial\mathscr{D}. \tag{2.5}$$

Thus they are solely determined by the geometric properties of the domain and can be computed in advance. For the channel domain considered here, Yang *et al.* (2010) have derived the basis functions analytically. A unique property of the helical bases is that each of them is a Beltramian field, i.e. the vector is parallel to its curl everywhere over the domain. The velocity field $\boldsymbol{v}=\boldsymbol{\phi}_s(\boldsymbol{x})$ corresponds to the vorticity field $\boldsymbol{\omega}=sk\boldsymbol{\phi}_s(\boldsymbol{x})$, which has the same vector lines as $\boldsymbol{v}$. Moreover, each basis is a steady solution of the inviscid Euler equation. Greenspan (1969) has used $\boldsymbol{\phi}_s(\boldsymbol{k},\boldsymbol{x})$ to construct the inviscid inertial wave solutions of rotating flow. In an infinite domain the streamlines of the helical basis take a helix-like form, see Waleffe (1993).

With the helical basis functions, the helical coefficients can be calculated as

$$\widehat{v}_s(\boldsymbol{k})=\int_{\mathscr{D}}\boldsymbol{v}(\boldsymbol{x})\cdot\boldsymbol{\phi}_s^*(\boldsymbol{k},\boldsymbol{x})\,\mathrm{d}\boldsymbol{x}, \tag{2.6}$$

where an asterisk denotes complex conjugate. The helical energy spectrum may also be defined by helical coefficients. Unlike homogeneous isotropic turbulence, generally the spectrum may depend on both the magnitude and direction of the wavenumber vector $\boldsymbol{k}$, and for the helical energy spectrum the polarity comes in as another new factor. In this paper we shall confine ourself to the effects of scale and polarity of the helical modes and ignore the effect of the direction of the wavenumber vector. The helical energy spectrum for single polarity can then be defined as

$$E_s(k)=\frac{1}{2}\sum_{|\boldsymbol{k}|\in I(k)}\widehat{u}_s(\boldsymbol{k})\widehat{u}_s^*(\boldsymbol{k}), \tag{2.7}$$

with $I(k)$ being an interval of the magnitude of the wavenumber vectors with midpoint k. The total spectrum is $E(k)=E_+(k)+E_-(k)$. For channel flow we only consider the spectrum of the fluctuating flow, which can be calculated by excluding the modes with $\boldsymbol{k}_\pi=0$, i.e. the modes which are constant on wall-parallel planes. Hereafter $\boldsymbol{k}_\pi$ stands for the wall-parallel component of wavenumber vector $\boldsymbol{k}$.

Write the fluctuating part of (2.1) as

$$\frac{\partial\boldsymbol{u}'}{\partial t}+\boldsymbol{l}'+2\boldsymbol{R}\times\boldsymbol{u}'=-\boldsymbol{\nabla}P'+\nu\nabla^2\boldsymbol{u}', \tag{2.8}$$

with the prime denoting fluctuating quantities. The fluctuating Lamb vector $\boldsymbol{l}'$ can be divided into

$$\boldsymbol{l}'=\boldsymbol{l}_1+\boldsymbol{l}_2+\boldsymbol{l}_3=\boldsymbol{\Omega}\times\boldsymbol{u}'+\boldsymbol{\omega}'\times\boldsymbol{U}+(\boldsymbol{\omega}'\times\boldsymbol{u}'-\overline{\boldsymbol{\omega}'\times\boldsymbol{u}'}), \tag{2.9}$$

where $\boldsymbol{U}$ and $\boldsymbol{\Omega}$ are the mean velocity and vorticity, and the overline denotes the average in homogeneous directions and time, respectively. Then applying HWD to (2.8) and multiplying the resulting equation by $\widehat{u}_s^*$, one gets

$$\frac{\partial E_s(k)}{\partial t}=\sum_i T_{is}(k)-D_s(k) \tag{2.10}$$

https://doi.org/10.1017/jfm.2011.500 Published online by Cambridge University Press

with $i = 1, 2, 3$ and

$$T_{is}(k) = -\sum_{|\boldsymbol{k}|\in I(k)}^{\boldsymbol{k}_\pi\neq\boldsymbol{0}} \mathrm{Re}[\widehat{l}_{is}(\boldsymbol{k})\widehat{u}_s^*(\boldsymbol{k})], \quad D_s(k) = \nu \sum_{|\boldsymbol{k}|\in I(k)}^{\boldsymbol{k}_\pi\neq\boldsymbol{0}} \mathrm{Re}[\widehat{d}_s(\boldsymbol{k})\widehat{u}_s^*(\boldsymbol{k})]. \tag{2.11}$$

Here $\widehat{l}_{is}$ and $\widehat{d}_s$ are the helical coefficients of $\boldsymbol{l}_i$ and $\boldsymbol{\nabla}\times\boldsymbol{\omega}$, Re stands for the real part of complex variables, the T_{is} represent different nonlinear mechanisms via which the energy is transferred into waveband $I(k)$, and D_s is the viscous dissipation. Once again we ignore the dependence of T and D on the direction of $\boldsymbol{k}$. The Coriolis term disappears in the energy equation, since it does not change the energy carried by a single helical mode, as proved by Yang *et al.* (2010). However, it will affect the nonlinear energy transfer, which will be discussed later with our numerical results.

3. Numerical results and discussion

3.1. *Numerical method and result validation*

Our DNS employs the standard pseudo-spectral method for channel flow simulation, as done by Kim, Moin & Moser (1987). For the temporal evolution the nonlinear and viscous terms are discretized by second-order explicit and implicit schemes, respectively. The Coriolis force is treated like the nonlinear terms. The 3/2-rule is utilized to remove the alias error. In our simulation we solve the second- and fourth-order equations for wall-normal components of vorticity and velocity, respectively. The flow was assumed to be driven by a constant gradient of the mean modified pressure $\overline{P}_m$ in the streamwise direction. The fluctuating part of the modified pressure P'_m is absent in the simulation.

It is well known that any conservative body force such as $\boldsymbol{\nabla}P_m$ does not appear in the vorticity equation but may affect the vorticity dynamics through the boundary condition. Since in the present formulation $\boldsymbol{\nabla}P_m$ is functionally orthogonal to any HWD bases and projected out, the P_m-related effects, such as fluctuating pressure, centrifugal force, and kinetic energy of the flow will be beyond our concern. Our discussion below is self-consistent, but we agree that those scalars are important in the momentum equation (Grundestam *et al.* 2008) and worth studying by using a different formulation without projection to solenoidal space.

For the spanwise rotating channel simulated here, the mean velocity profile $U(y)$ becomes asymmetric about the centreline, and hence so are the wall-friction velocities, which are denoted by u_τ^b and u_τ^t at the bottom and top walls, respectively. Two Reynolds numbers, Re_τ^b and Re_τ^t, can then be defined accordingly. Also a unified wall-friction velocity can be defined as (Grundestam *et al.* 2008)

$$u_\tau = \sqrt{(u_\tau^b)^2/2 + (u_\tau^t)^2/2}. \tag{3.1}$$

All the quantities in our study are non-dimensionalized by the channel half-height h and u_τ. Hereafter the subscript τ denotes quantities calculated with u_τ. A series of simulations have been carried out with different rotation numbers. For all simulations L_x and L_z are fixed to $4\pi h$ and $2\pi h$ with $h = 1$, and the resolution is $128\times129\times128$ for $Ro \leqslant 30$ and increases to $192\times193\times192$ for $Ro = 40$. We are aware that the present resolutions are limited for the wall-friction velocity in some cases, especially at the suction side. Nevertheless, the domain size and the wall-normal resolution for similar Ro are comparable with those in Grundestam *et al.* (2008). All the simulations start from an instantaneous field extracted from a non-rotating channel simulation.

https://doi.org/10.1017/jfm.2011.500 Published online by Cambridge University Press

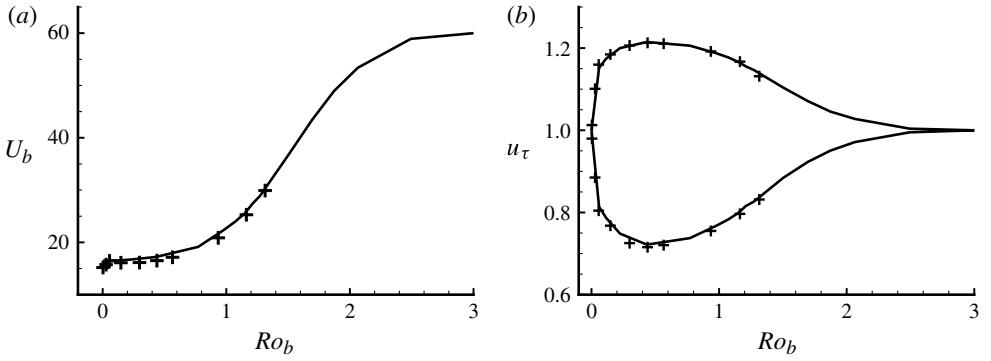


FIGURE 2. Comparison between our results (symbols) and those in Grundestam *et al.* (2008) (lines). In (*b*) the upper branch is u_τ^b at the pressure side, and the lower branch is u_τ^t at the suction side.

Case	Ro	Ro_b	Re_τ^b	Re_τ^t	Re_b
SP001	0.1	0.006 39	183.1	177.2	2813.7
SP005	0.5	0.0309	199.0	160.1	2914.3
SP01	1.0	0.0592	209.6	145.6	3041.3
SP02	2.5	0.151	214.1	139.1	2979.7
SP05	5.0	0.302	218.0	131.5	2984.9
SP07	7.5	0.442	219.1	129.6	3052.2
SP10	10.0	0.568	218.7	130.5	3166.6
SP20	20.0	0.938	215.4	136.7	3836.5
SP30	30.0	1.166	210.9	144.2	4630.5
SP40	40.0	1.318	204.5	150.5	5464.2

TABLE 1. Rotation numbers and Reynolds numbers for all simulated cases.

After the flow becomes statistically steady, i.e. the kinetic energy fluctuates around some constant, the flow statistics are sampled over a time duration of $40h/u_\tau$. This sampling time is shorter than that of Grundestam *et al.* (2008) (over $100h/u_\tau$). To verify the adequacy of our resolutions and the time duration for sampling, let us compare the results with those of Grundestam *et al.* (2008). The parameters of the DNS and several statistics are listed in table 1, in which the subscript b stands for the quantities calculated with the bulk velocity

$$U_b = \frac{1}{2h}\int_{-h}^{h} U(y)\,\mathrm{d}y. \tag{3.2}$$

U_b, u_τ^b and u_τ^t are compared to the results of Grundestam *et al.* (2008) in figure 2. The agreement is very good. As Ro increases, U_b also increases. Both u_τ^b and u_τ^t change non-monotonically with opposite trends. They reach extrema between $Ro = 7.5$ and 10. In figure 3 we show the mean streamwise velocity for different Ro. For the smallest rotation rate, the linear segment is rather short. For the other cases, the linear segments with slope of $2R$ are very clear. The linear region shifts towards the pressure side as Ro increases.

https://doi.org/10.1017/jfm.2011.500 Published online by Cambridge University Press

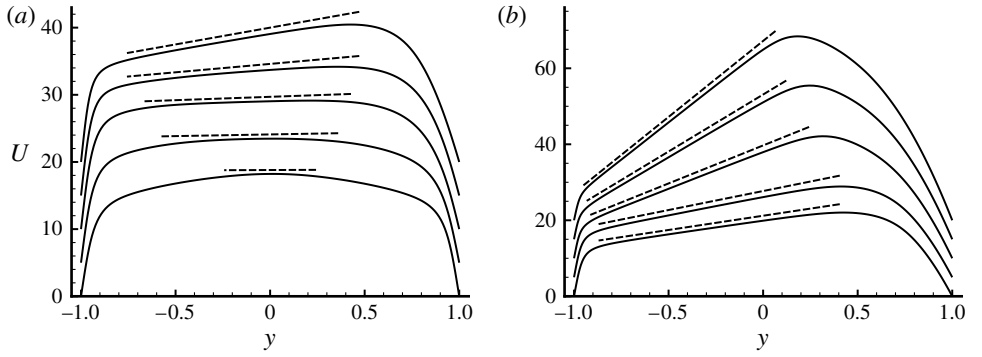


FIGURE 3. The mean velocity profiles. The dashed lines have the slope of $2R$. *Ro* increases from bottom to top, and for clarity each curve is shifted upward from the previous one by 5. $y = -1$ is the pressure side and $y = 1$ the suction side. (*a*) SP001–SP05, (*b*) SP07–SP40.

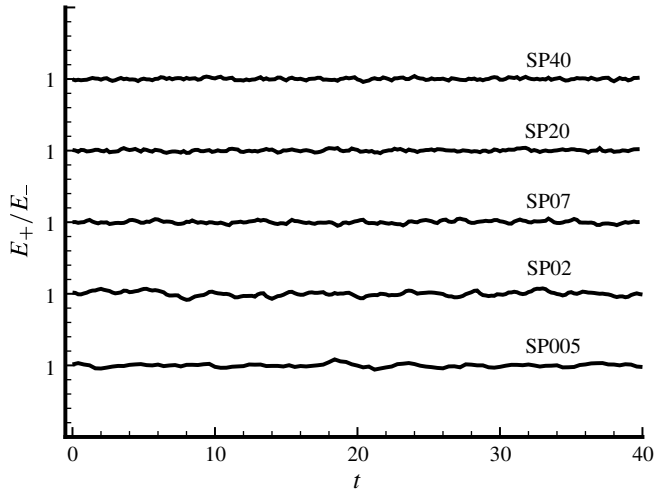


FIGURE 4. The time history of E_+/E_- for five rotation rates.

3.2. *Helical energy spectra and flow structures*

During DNS, flow fields have been stored to conduct the numerical HWD. The spectrum defined in (2.7) has been computed for all cases. We set the width of $I(k)$ to be $\pi/2$, which is the step size of k_y in the wall-normal direction. Results indicate that the channel flow with spanwise rotation remains symmetric between two opposite polarities, or statistically $E_+ \approx E_-$, as shown in figure 4. This is very different from the streamwise rotating channel studied by Yang *et al.* (2010), the reasons for which will be discussed later in § 3.4.

Owing to the polarity-symmetry, hereafter we will ignore the effect of the polarity. The fluctuating energy spectra $E(k)$ for different *Ro* are plotted in figure 5. The same spectrum of the non-rotating case is also plotted for comparison. Clearly, once the channel is subjected to a very slow rotation, the location of the maximum in energy spectrum starts to shift towards the small k. Then as *Ro* increases, saying $Ro > 2$, the most energetic scale moves back towards large wavenumbers. For $Ro > 20$, the wavenumber carrying maximal energy is already larger than that of the non-

https://doi.org/10.1017/jfm.2011.500 Published online by Cambridge University Press

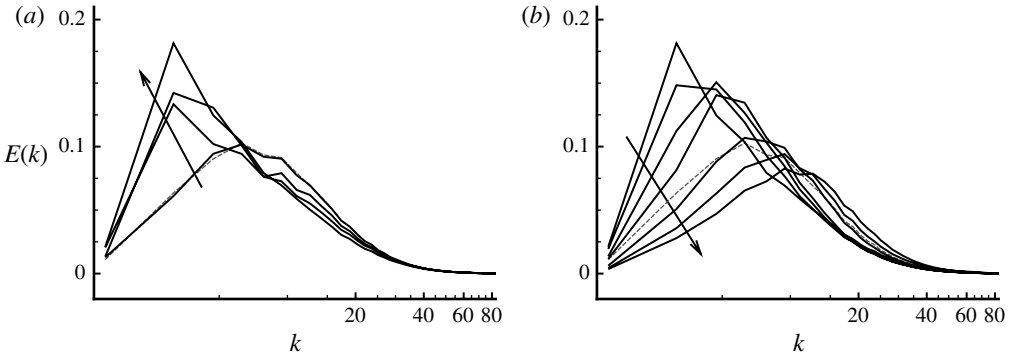


FIGURE 5. The time-averaged helical spectra for different Ro, normalized by the corresponding total fluctuating energy $E_a = \sum_{s,k} E_s(k)$. Dashed grey line: non-rotating case; solid lines: SP cases. The arrow indicates the direction of increasing Ro. The spectrum of SP02, which has the highest peak, is shown in both figures for reference: (*a*) SP001 to SP02; (*b*) SP02 to SP40.

rotating case. This variation of $E(k)$ versus Ro strongly suggests that for slow rotation some large-scale structures emerge in the channel; while as rotation strengthens, the fluctuating structures are excited at gradually smaller scales.

To investigate the flow structures in physical space, we use the Q-criterion proposed by Hunt, Wray & Moin (1988) to identify the vortices. For cases SP02 and SP40, figure 6 depicts the vortical structures in the region between the bottom wall and the location where U reaches maximum, which covers the linear segment of U. We have already shown in figure 5 that the energy concentrates to very large scales for SP02 and relatively small scales for SP40. Consistent with this finding, the vortical structures of the two cases exhibit very different shapes. For $Ro = 2$ the fine vortical structures gather into clusters, each of which forms a long column basically in the streamwise direction. These large columns cannot be found for $Ro = 40$, see figure 6(*b*). Instead, for SP40 the thin vortices seem to align and extend over very long distance in the streamwise direction.

The columns in figure 6(*a*) are relevant to the roll cells reported in the previous studies. Following Kristoffersen & Andersson (1993) and Grundestam *et al.* (2008), we average the flow field shown in figure 6(*a*) in the streamwise direction and plot the flow patterns on the cross-section in figure 7. Clearly, the closed projection of x-averaged streamlines identify two pairs of large counter-rotating roll cells, as well as some small ones. The rotating directions of the roll cells are consistent with the background contours of the streamwise-averaged $\widetilde{\omega}_x$. Namely, they rotate in the clockwise direction when $\widetilde{\omega}_x > 0$ (the light region), and in the counterclockwise direction when $\widetilde{\omega}_x < 0$ (the dark region). The locations of the roll cells coincide with those of the columnar vortex clusters in figure 6(*a*). Specifically, the two pairs of large roll cells at $1 < z < 3$ and $4 < z < 6$ correspond to the two long columns in figure 6(*a*) expanding over entire channel length. The small ones around $z = 0.4$ and 3.4 are probably related to the shorter columns at the same spanwise location in figure 6(*a*).

3.3. *The nonlinear energy transfer*

We now investigate the nonlinear energy transfer between different helical modes. Since the flow is polarity-symmetric, it is sufficient to consider $T_i(k) = \sum_s T_{is}(k)$

https://doi.org/10.1017/jfm.2011.500 Published online by Cambridge University Press

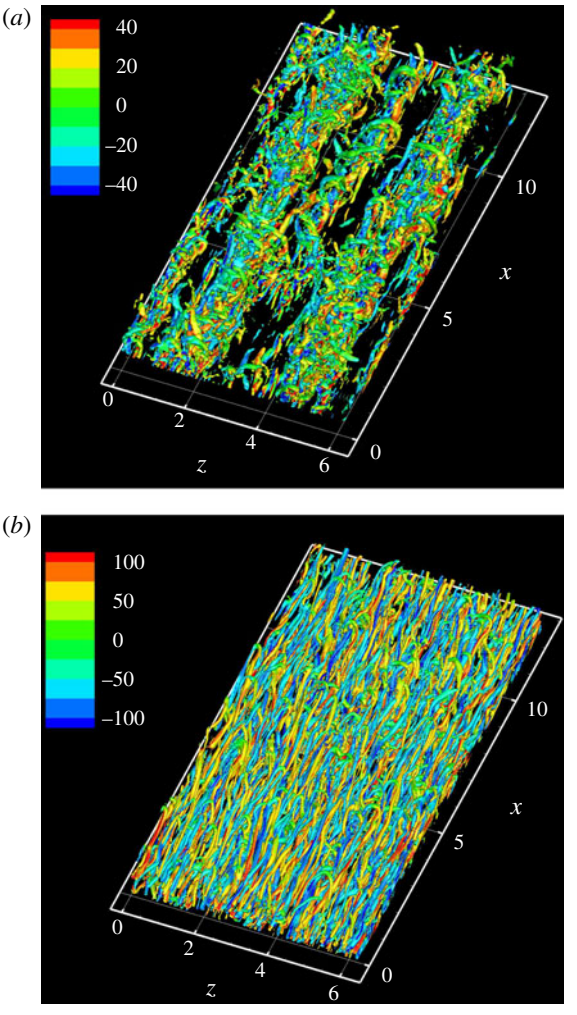


FIGURE 6. Vortical structures illustrated by the iso-surface $Q = 1\%\, Q_{max}$ between the bottom wall and the layer with largest mean streamwise velocity, and coloured by the contours of the instantaneous streamwise vorticity ω_x: (*a*) SP02; (*b*) SP40.

with $T_{is}(k)$ defined in (2.11). The energy flows into (out from) waveband $I(k)$ if $T_i(k)$ is positive (negative). By the definitions of their counterparts $\boldsymbol{I}_i$ in the physical space, T_1 and T_2 may be interpreted as the rates at which the energy is transferred into waveband $I(k)$ due to the interaction between the mean flow and fluctuating modes, and T_3 corresponds to the interaction of the fluctuating modes. Moreover, as explained in Yang *et al.* (2010), one has $\sum_k T_1(k) = \sum_k T_3(k) = 0$ and statistically $\sum_k T_2(k) = \sum_{k,s} D_s(k)$. These equalities imply that the T_1 and T_3 terms do not change the total fluctuating energy but only redistribute the energy among different modes, and the T_2 term represents a mechanism by which the fluctuating flow extracts energy from the mean flow. This energy finally dissipates through viscosity.

The transfer functions are shown in figure 8, together with the total transfer function $T_a = T_1 + T_2 + T_3$. Basically, T_2 is positive for all wavenumbers, while T_1 is negative for small k and positive for large k. These together imply that the nonlinear interaction

https://doi.org/10.1017/jfm.2011.500 Published online by Cambridge University Press

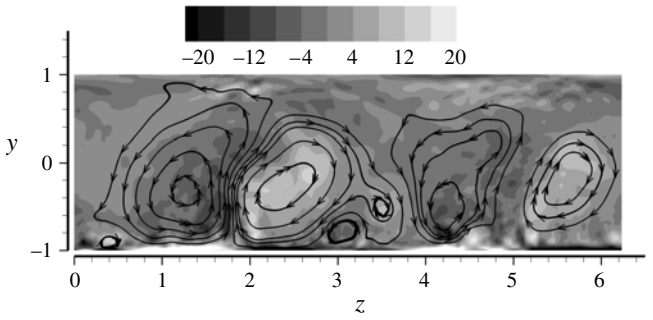


FIGURE 7. The flow pattern depicted by the streamwise-averaged streamlines on the (y, z)-plane at the same time step as figure 6(*a*). The background contours are the streamwise vorticity $\widetilde{\omega}_x$ averaged in the x-direction.

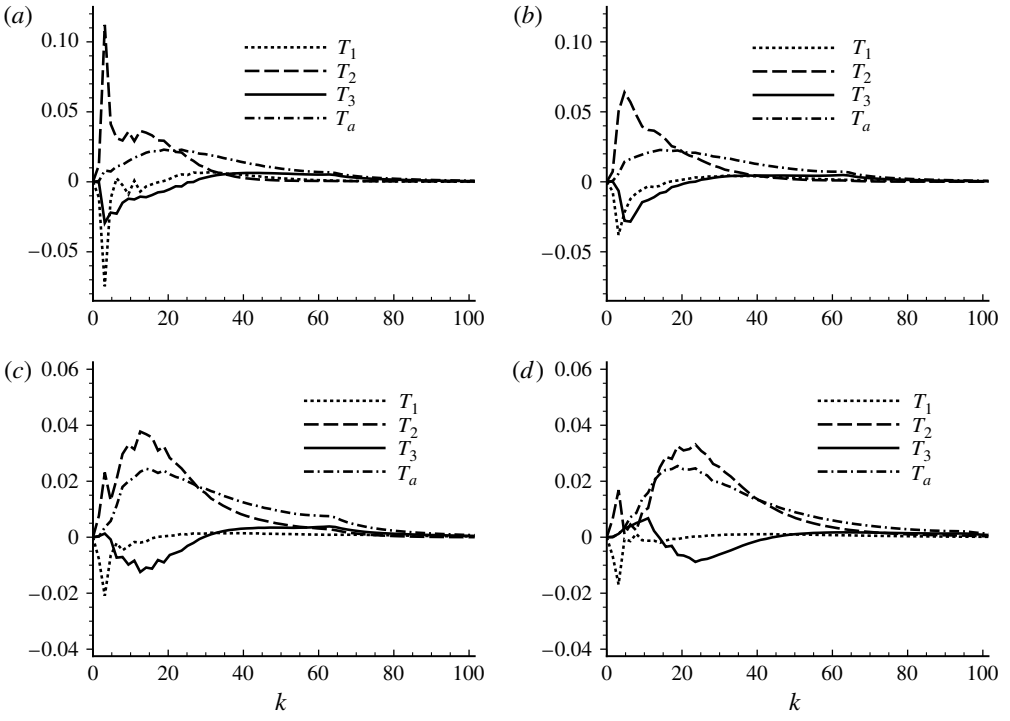


FIGURE 8. The time-averaged transfer functions $T_i(k)$ and $T_a(k)$ for four rotation rates, normalized by total dissipation. Note in (*a*) and (*b*) the range of ordinates is twice that in (*c*) and (*d*): (*a*) SP02; (*b*) SP07; (*c*) SP20; (*d*) SP40.

between the mean flow and the fluctuating flow has two kinds of effects. Firstly, all the fluctuating modes gain energy which can only come from the mean flow, as depicted by T_2. Secondly, the energy is redistributed among different modes which is reflected by T_1. As Ro increases, the location of the T_2-peak varies in a way similar to that of the energy spectrum. With slow rotation large-scale modes obtain energy at higher rate, while when rotation rate increases the largest transfer occurs at smaller scales.

https://doi.org/10.1017/jfm.2011.500 Published online by Cambridge University Press

This picture is consistent with the dominant scales of vortical structures at different Ro values, see figure 6.

The behaviour of T_1 is completely different from that of T_2. The T_1-minimum is always located at a fixed small k for all four rotation rates. Interestingly, a second T_2-peak appears at the same small wavenumber for two larger rotation numbers in figures 8(c) and 8(d). These opposite peaks of T_1 and T_2 cancel each other so that no net effect shows on the T_a curves. As illustrated by Grundestam *et al.* (2008), for fast rotating cases the only large-scale structures emerging in the flow fields are the elongated and slanted structures of the fluctuating streamwise velocity component u', which may be the physical phenomena responsible for the T_1-minimum and secondary T_2-peak. However, at this point we do not have conclusive evidence for the link between them.

The interaction of the fluctuating modes reflected by T_3 has more interesting behaviour. For weak rotation, T_3 is negative at small k and positive at large k. This is similar to homogeneous isotropic flow, where the nonlinear interactions of the fluctuating modes transfer energy from large scales to small ones. However, for strong rotation T_3 becomes positive at those smallest wavenumbers, meaning that the large scales begin to receive energy. To illustrate this phenomenon more clearly, one can define an energy flux function associated with T_3 as

$$\Pi(K) = \sum_{k>K} T_3(k), \tag{3.3}$$

which represents the energy flux through wavenumber K to all the modes with $k > K$ by the nonlinear interaction of the fluctuating modes. In figure 9 we plot $\Pi(K)$ for all cases. Evidently, a region with $\Pi(K) < 0$ appears at small K and extends rightward as Ro increases. The negative $\Pi(K)$ means the energy flux through K is from small to large scales and thus signals an inverse energy cascade. In other words, with strong rotation the nonlinear interaction among the fluctuating modes causes the energy to move from small to large scales.

By analysing the transport equations of the Reynolds stress, Grundestam *et al.* (2008) demonstrated that the inverse energy cascade existed in a spanwise rotating channel, i.e. the production term of turbulent kinetic energy could be negative in a layer adjacent to the location with maximal U at the stable side. The energy was fed back to the mean flow at this region. However, this observation is not the same phenomenon as the 'inverse cascade' we discussed above. While Grundestam *et al.* (2008) considered the energy transfer between the mean flow and the turbulent fluctuation, figure 9 suggests that the pure fluctuating energy may be transferred from small scales to the larger ones. Thus the inverse cascade reported here is unlikely to be related to the relaminarization at the stable side of the channel. In other words, for sufficiently large Ro a certain mechanism appears that can create large-scale structures. One such candidate will be proposed in the next section.

3.4. *The effects of the Coriolis force*

Since the centrifugal effect has been absorbed into the modified pressure term, in our model problem the only effect introduced by rotation is the Coriolis force. Thus it must be the Coriolis force that causes the interesting behaviour of the vortical structures different from the non-rotating cases. To study the effect of the Coriolis force, we investigate the mean and fluctuating parts separately. We employ the hairpin vortex as a model structure, since it may explain many observations in wall-turbulence studies (Adrian 2007). Consider a single hairpin vortex at the pressure side. Its

https://doi.org/10.1017/jfm.2011.500 Published online by Cambridge University Press

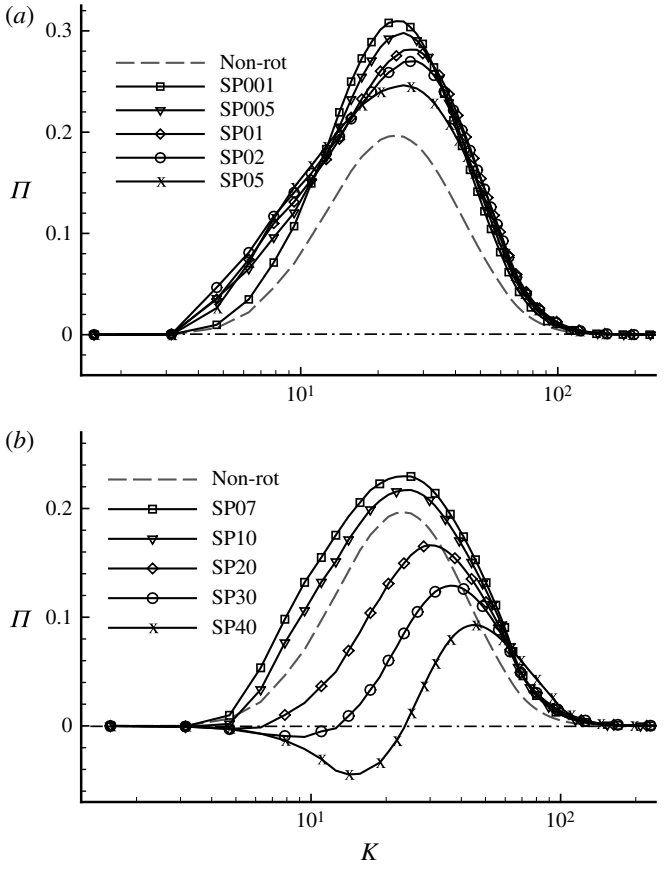


FIGURE 9. Time-averaged energy flux function $\Pi(K)$ for all cases, normalized by total dissipation. The horizontal dash-dotted line marks $\Pi = 0$. The non-rotating case is also shown for comparison: (*a*) SP001-SP05; (*b*) SP07-SP40.

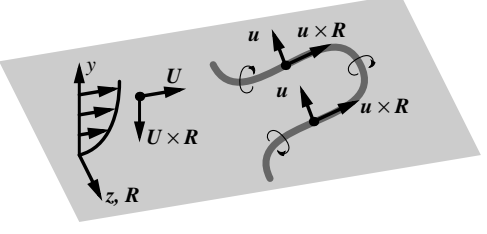


FIGURE 10. Illustration of the acceleration due to the Coriolis force for average and fluctuating motion at the pressure side.

advection velocity may be decomposed into two parts: the velocity $\boldsymbol{U}$ associated with the mean flow and the self-induced fluctuating velocity. For the mean flow $\boldsymbol{U}$ at the pressure side, as shown in figure 10, the Coriolis acceleration $2\boldsymbol{U} \times \boldsymbol{R}$ points towards the wall. This causes the incline angles of the hairpin vortices to decrease from the 45° of the non-rotating case to a smaller value, which has been confirmed by Lamballais *et al.* (1996).

https://doi.org/10.1017/jfm.2011.500 Published online by Cambridge University Press

For the fluctuating part, the two near-parallel legs of the hairpin vortex have opposite axial vorticity, and the velocity $\boldsymbol{u}$ of each leg induced by the vorticity of the other one is perpendicular to the leg and points back upward. The Coriolis acceleration associated with this velocity is parallel to the leg and points forward. Thus, the Coriolis force causes axial stretching of the two legs. The larger the induced velocity is, the stronger is the stretching. Similar analysis can be done at the suction side. Now the Coriolis force caused by the mean velocity points away from the upper wall. And the Coriolis force associated with the self-advection of the hairpin legs is still along the legs but in the direction opposite to that shown in figure 10. This force may prevent the elongation of the hairpin legs at the suction side and thus reduce the production of turbulence.

Of course in turbulent flow the situation is much more complicated. Robinson (1991) has thoroughly reviewed the coherent vortical structures in a turbulent boundary layer and concluded that quasi-streamwise vortices are more commonly observed than complete hairpin vortices in the near-wall region. Adrian (2007) noted that the hairpins often occurred in the logarithmic layer. Recently, Wu & Moin (2009) simulated a zero-pressure-gradient flat-plate boundary layer, including both the transition and fully developed regions. The results confirmed the preponderance of the hairpin-like structures, which had never been reported in a channel simulation, probably due to the periodic condition (Wu & Moin 2009).

In our simulations, owing to the low Reynolds number and the periodicity in the streamwise direction, the vortical structures often take a quasi-streamwise form rather than a hairpin shape, as shown in figure 6(*b*). Nevertheless, we calculated the time-averaged probability density function (p.d.f.) of the cosine of the angle spanned by the fluctuating Coriolis force $2\boldsymbol{u} \times \boldsymbol{R}$ and the fluctuating vorticity $\boldsymbol{\omega}$, i.e. $\cos\alpha = (2\boldsymbol{u} \times \boldsymbol{R}) \cdot \boldsymbol{\omega}/(|2\boldsymbol{u} \times \boldsymbol{R}||\boldsymbol{\omega}|)$. In figure 11 the p.d.f. $P(y, \cos\alpha)$ is plotted for four cases in the region between $-0.99 < y < 0.99$. We avoid the near-wall region where the fluctuating velocity is too small to compute $\cos\alpha$ accurately. Evidently, two distinct regions appear in all figures. At the suction side (the upper part) a single peak is located at $\cos\alpha = 0$, while at the pressure side (the lower part) there are two peaks at $\cos\alpha = \pm 1$. The boundaries between the two regions coincide with the locations of the upper ends of the linear segments in figure 3.

The single peak at the suction side is because the wall-normal components of the fluctuating velocity and vorticity decrease to nearly zero in this region as Ro becomes larger. Thus $\boldsymbol{u} \times \boldsymbol{R}$ is basically in the wall-normal direction and $\boldsymbol{\omega}$ parallel to the wall, which implies that $\cos\alpha$ tends to be zero. At the pressure side, two ridges with large p.d.f. value appear at $\cos\alpha = \pm 1$. As Ro increases the two ridges become increasingly stronger and sharper, and the p.d.f. value around $\cos\alpha = 0$ decreases. That is, for fluctuating flow the Coriolis force tends to align with the vorticity lines as the rotation is enhanced. Naturally, this 'axial' Coriolis force can either stretch or shrink the vortices. Therefore the Coriolis force may effectively change the scale of the vortical structures. If some vortices are stretched significantly, large-scale structures emerge, which can be a mechanism for the inverse energy cascade. Another interesting observation is that in the y-direction, the ridges of P at $\cos\alpha = \pm 1$ are located in the range of the linear segments of $U(y)$, where the absolute mean vorticity is near zero. This implies that the Coriolis-force stretching/shrinking mainly occurs in the region where $U(y)$ is linear.

Finally, we would like to discuss the different scenarios for the spanwise and streamwise rotating cases. For spanwise rotation, as explained above the two legs of the hairpin vortex experience a Coriolis force of the same direction. However, this

https://doi.org/10.1017/jfm.2011.500 Published online by Cambridge University Press

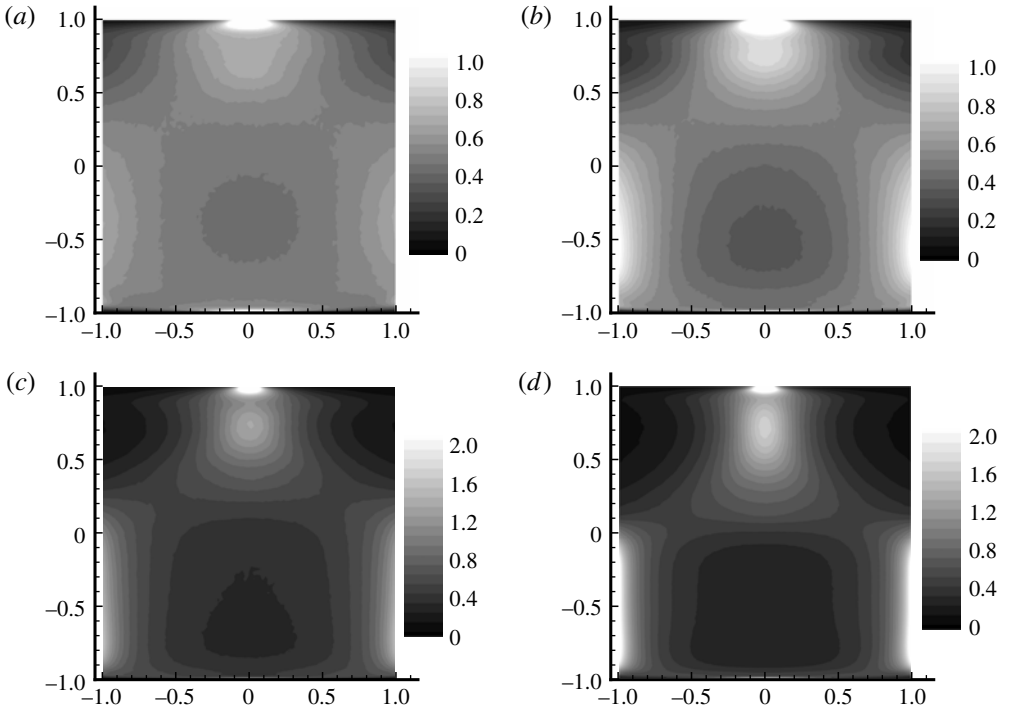


FIGURE 11. Normalized probability density function $P(y, \cos\alpha)$ for different rotation rates. Note that the range of grey scales for the lower row is twice that of the upper row: (*a*) SP02; (*b*) SP07; (*c*) SP20; (*d*) SP40.

is not the case in the streamwise rotating case. Again referring to figure 10, for streamwise rotation $\boldsymbol{R}$ is in the x-direction as is $\boldsymbol{U}$. Thus the Coriolis force associated with the fluctuating velocity $\boldsymbol{u}$ of the vortex legs should be in the negative (or positive) z-direction at the pressure (or suction) side. This will twist the hairpin structure laterally, which may stretch one leg and prevent the development of the other one. Thus the symmetry of positive and negative ω_x can be broken by the Coriolis force in the streamwise rotating case. For instance, near the lower wall as shown in figure 10, the Coriolis force points to left (when one faces the main flow direction) and the right leg with positive ω_x is stretched. The positive ω_x should exceed the negative ω_x. This analysis is consistent with the observation in Yang *et al.* (2010), who found that the skewness of ω_x is positive in this region.

4. Conclusions

In this paper we have investigated turbulent channel flow with spanwise rotation by DNS and HWD. HWD provides us a full-scale decomposition for wall-bounded channel flow. The helical energy spectra indicate that structures with large scales exist at small rotation number. Flow visualizations imply that the fine vortical structures cluster into long columns, which are related to the roll cells reported in the previous literature. The maximum of the energy spectrum shifts towards larger wavenumber as rotation becomes stronger. Accordingly, at strong rotation the fine vortical structures appear as thin long vortices which are basically along the streamwise direction.

https://doi.org/10.1017/jfm.2011.500 Published online by Cambridge University Press

The nonlinear energy transfer is then investigated by the transfer function. As *Ro* increases, smaller fluctuating scales obtain energy from the mean flow more efficiently. The nonlinear interactions of the fluctuating modes can induce negative energy flux through small wavenumber when rotation is strong enough, which suggests the occurrence of an inverse energy cascade within the fluctuating part of the flow. The effect of the Coriolis force on the flow structures has also been studied in the physical space. The Coriolis acceleration associated with the mean flow suppresses the inclination of the hairpin vortices at the pressure side. At the same time, the Coriolis acceleration associated with the fluctuating velocity tends to be parallel to the fluctuating vorticity vector for large rotation numbers. Therefore, strong axial stretching/shrinking may be exerted on the streamwise vortices by the fluctuating Coriolis force, which can change the scale of the vortical structures significantly and provide a mechanism for the inverse energy cascade.

Open issues remain in the present study and are worth investigating in the future. An important though untouched problem is the role of the pressure in the flow. Grundestam *et al.* (2008) argued that the pressure–strain correlation can redistribute the wall-normal fluctuations to the streamwise component. Pressure is also absent in our phenomenological analysis in § 3.4, which will be studied in our future work.

Acknowledgements

The authors appreciate the insightful discussion with Professor M.-D. Zhou and the valuable comments of the referees. This work was supported in part by the National Natural Science Foundation of China, Key Project No. 10532010, the Ministry of Science and Technology of China's Turbulence Program under Grant No. 2009CB724101, and National Natural Science Foundation of China (Grant No. 10921202). Y.-T.Y. also acknowledges the partial support by the National Science Foundation under Grant No. NSF PHY05-51164. The numerical simulations were conducted on the HP clusters at the Center of Computational Science and Engineering and the College of Engineering, Peking University.

REFERENCES

ADRIAN, R. J. 2007 Hairpin vortex organization in wall turbulence. *Phys. Fluids* **19**, 041301.

ALFREDSSON, P. H. & PERSSON, H. 1989 Instabilities in channel flow with system rotation. *J. Fluid Mech.* **202**, 543–557.

GREENSPAN, H. P. 1969 *The Theory of Rotating Fluids*. Cambridge University Press.

GRUNDESTAM, O., WALLIN, S. & JOHANSSON, A. V. 2008 Direct numerical simulations of rotating turbulent channel flow. *J. Fluid Mech.* **598**, 177–199.

HUNT, J. C. R., WRAY, A. A. & MOIN, P. 1988 Eddies, stream, and convergence zones in turbulent flows. *Center for Turbulence Research Rep.* CTR-S88, pp. 193–208.

JOHNSTON, J. P., HALLEEN, R. M. & LEZIUS, D. K. 1972 Effects of spanwise rotation on the structure of two-dimensional fully developed turbulent channel flow. *J. Fluid Mech.* **56**, 533–557.

KIM, J., MOIN, P. & MOSER, R. 1987 Turbulence statistics in fully-developed channel flow at low Reynolds number. *J. Fluid Mech.* **177**, 133–166.

KRISTOFFERSEN, R. & ANDERSSON, H. 1993 Direct simulations of low-Reynolds-number turbulent-flow in a rotating channel. *J. Fluid Mech.* **256**, 163–197.

LAMBALLAIS, E., LESIEUR, M. & MÉTAIS, O. 1996 Effects of the spanwise rotation on the vorticity stretching in transitional and turbulent channel flow. *Intl J. Heat Fluid Flow* **17**, 324–332.

https://doi.org/10.1017/jfm.2011.500 Published online by Cambridge University Press

LAMBALLAIS, E., MÉTAIS, O. & LESIEUR, M. 1998 Spectral-dynamic model for large-eddy simulations of turbulent rotating channel flow. *Theor. Comput. Fluid Dyn.* **12**, 19–177.

NAKABAYASHI, K. & KITOH, O. 2005 Turbulence characteristics of two-dimensional channel flow with system rotation. *J. Fluid Mech.* **528**, 355–377.

ROBINSON, S. K. 1991 Coherent motions in the turbulent boundary layer. *Annu. Rev. Fluid Mech.* **23**, 601–639.

TAKFTI, D. K. & VANKA, S. P. 1991 A numerical study of the effects of spanwise rotation on turbulent channel flow. *Phys. Fluids* A **3** (4) 6420–656.

WALEFFE, F. 1993 Inertial transfers in the helical decomposition. *Phys. Fluids* A **5** (3), 677–685.

WALL, D. P. & NAGATA, M. 2006 Nonlinear secondary flow through a rotating channel. *J. Fluid Mech.* **564**, 25–55.

WU, X. H. & MOIN, P. 2009 Direct numerical simulation of turbulence in a nominally zero-pressure-gradient flat-plate boundary layer. *J. Fluid Mech.* **630**, 5–41.

YANG, Y. T., SU, W. D. & WU, J. Z. 2010 Helical wave decomposition and applications to channel turbulence with streamwise rotation. *J. Fluid Mech.* **662**, 91–122.

https://doi.org/10.1017/jfm.2011.500 Published online by Cambridge University Press